

CSI-EPT: A Contrast Source Inversion Approach for Improved MRI-Based Electric Properties Tomography

Edmond Balidemaj*, Cornelis A.T. van den Berg, Johan Trinks, Astrid L.H.M.W. van Lier, Aart J. Nederveen, Lukas J. A. Stalpers, Hans Crezee, and Rob F. Remis

Abstract—Electric properties tomography (EPT) is an imaging modality to reconstruct the electric conductivity and permittivity inside the human body based on B_1^+ maps acquired by a magnetic resonance imaging (MRI) system. Current implementations of EPT are based on the local Maxwell equations and assume piecewise constant media. The accuracy of the reconstructed maps may therefore be sensitive to noise and reconstruction errors occur near tissue boundaries. In this paper, we introduce a multiplicative regularized CSI-EPT method (contrast source inversion—electric properties tomography) where the electric tissue properties are retrieved in an iterative fashion based on a contrast source inversion approach. The method takes the integral representations for the electromagnetic field as a starting point and the tissue parameters are obtained by iteratively minimizing an objective function which measures the discrepancy between measured and modeled data and the discrepancy in satisfying a consistency equation known as the object equation. Furthermore, the objective function consists of a multiplicative Total Variation factor for noise suppression during the reconstruction process. Finally, the presented implementation is able to simultaneously include more than one B_1^+ data set acquired by complementary RF excitation settings. We have performed *in vivo* simulations using a female pelvis model to compute the B_1^+ fields. Three different RF excitation settings were used to acquire complementary B_1^+ fields for an improved overall reconstruction. Numerical results illustrate the improved reconstruction near tissue boundaries and the ability of CSI-EPT to reconstruct small tissue structures.

Index Terms—B1 map, EPT, electric properties tomography, dielectric tissue mapping, MRI, contrast source inversion, conductivity, permittivity, SAR.

Manuscript received December 19, 2014; revised February 06, 2015; accepted February 12, 2015. Date of publication February 20, 2015; date of current version August 28, 2015. The research presented in this paper was supported by the Dutch Cancer Society (Grant: UVA 2010-4660). *Asterisk indicates corresponding author.*

*E. Balidemaj is with the Radiotherapy and Radiology Department, University of Amsterdam, Academic Medical Center, 1105AZ Amsterdam, The Netherlands (e-mail: e.balidemaj@amc.nl).

J. Trinks, A. Nederveen, L. Stalpers, and H. Crezee are with the Radiotherapy and Radiology Department, University of Amsterdam, Academic Medical Center, 1105AZ Amsterdam, The Netherlands.

C. A. T. van den Berg and A. van Lier are with the Radiotherapy Department, Utrecht University, University Medical Center, 3508 GA Utrecht, The Netherlands.

R. Remis is with the Circuits and Systems Group, Delft University of Technology, Faculty of Electrical Engineering, Mathematics and Computer Science, 2828CD Delft, The Netherlands.

Digital Object Identifier 10.1109/TMI.2015.2404944

I. INTRODUCTION

ELECTRIC PROPERTIES (EPs) of biological tissues, consisting of the conductivity (σ) and permittivity (ϵ), are essential to determine the Specific Absorption Rate (SAR) and radiofrequency (RF) electromagnetic fields that play an essential role in MR imaging and hyperthermia treatment [1]. EPs may also provide diagnostic information related to physiological and pathological conditions of tumors and healthy tissues [2]–[8]. Previous studies have shown the feasibility of retrieving the electric tissue properties from measured B_1^+ field maps. A first paper appeared in 1991 by Haacke [9], where he proposed a non-invasive technique to retrieve the tissue electric properties from MR data. Later, electric properties reconstruction with phantom and animal experiments at 1.5 T and 4.7 T were presented in [10]. More recently, Electric Properties Tomography (EPT) [11] was introduced as a means of retrieving the conductivity and permittivity of different tissue types based on measured transmit B_1^+ amplitude and phase maps. Furthermore, the feasibility of EPT in the human head using B_1^+ phase only information has been demonstrated in [12], [13] and in [14] the so-called Local Maxwell Tomography (LMT) technique was introduced, which is free of assumptions regarding the B_1^+ phase. A similar phase assumption-free approach was also described in [15]. Finally, the feasibility of EPT of pelvic tumors was recently shown [16] for use in Hyperthermia Treatment Planning. These currently used methods are based on local field equations (either Maxwell's equations or Helmholtz's equation) for tissue parameter retrieval and most of them assume piecewise constant media. Since the electromagnetic boundary conditions are not explicitly taken into account, the reconstructed dielectric maps are unreliable near tissue boundaries. Furthermore, the currently used methods are sensitive to noise, since spatial differentiation operators act on generally noisy B_1^+ data. It has been shown that the boundary error is fundamental and can lead to misinterpretation of EPT images of inhomogeneous objects [17]. Recent studies have focused on minimizing the boundary error by obtaining the gradient of EPs using multi-channel transmit/receive array RF coil [18] or by using arbitrary-shaped kernels based on voxel position [19] instead of using a Gaussian-filtered Laplacian. In [20], an EPT method based on convection-reaction equation is introduced which is solved using a triangular mesh based finite difference method. However, these studies are based on differentiation operators as well. For an improved

overall reconstruction and specifically at tissue boundaries, a novel approach (CSI-EPT: Contrast Source Inversion—Electric Properties Tomography) to tissue parameter retrieval was recently presented in [21]–[23]. This approach is based on the Contrast Source Inversion (CSI) method as introduced in [24]. The CSI method has been applied for oil explorations purposes [25] and later for tissue properties mapping in [26] where a 2.33-GHz circular microwave scanner was used. In these applications, CSI is based on EM measurements performed outside the object of interest. An MRI system, however, offers the unique situation in which the B_1^+ fields within the object of interest can be measured. Here, every measured voxel can be considered as a virtual receiving antenna and consequently CSI-EPT was able to reconstruct high-accuracy dielectric tissue maps of interior parts of the human body based on noiseless B_1^+ data [22]. As opposed to the local methods mentioned above, CSI-EPT takes the global integral representations for the electromagnetic field quantities as a starting point. The boundary conditions are then automatically taken into account and the method is less sensitive to noise since integral operators (instead of differential operators) act on the measured field data.

In this work, a multiplicative regularized CSI-EPT method is introduced which exploits the abundance of magnetic field information. The effects of noisy B_1^+ data are suppressed by the introduction of a multiplicative regularization term in the objective function. Furthermore, the possibility of including multiple B_1^+ field data sets in the iterative process has been implemented. The various B_1^+ field data sets are acquired by complementary antenna RF excitation settings and can be simultaneously used in the iterative CSI-EPT process leading to an overall improvement of the reconstructed dielectric values. The current work is a theoretical evaluation in which we consider a two-dimensional configuration without RF shield and assume a known distribution of the B_1^+ phase. According to [27], a two-dimensional configuration provides a good approximation of the fully vectorial three-dimensional field inside a pelvic region that is situated in the midplane of a 3 T and 7 T body coil. The CSI-EPT method presented here is applicable for electric properties mapping at arbitrary magnetic field strength, however, in this work we present the results for a 3 T MRI.

Throughout this paper we use subscript notation and the Einstein summation convention applies (implicit summation over repeated subscripts). Subscripts refer to spatial indices and do not label channel numbers, for example. The conductivity $\sigma(\mathbf{x})$ and permittivity $\varepsilon(\mathbf{x})$ at the Larmor frequency ω are assumed to be isotropic and dependent on the position $\mathbf{x} = (x_1, x_2, x_3)$. We have ignored relative permeability (μ_r) variations as they are considered small for biological tissue [31]. Furthermore, a time factor $\exp(-i\omega t)$ was used in this paper in order to conform with current practice in MRI engineering.

II. BASIC EQUATIONS

Let us start by considering the RF field that is present within an MRI scanner in absence of a dielectric object or body. We call this field the electromagnetic background field and denote it as $\{E_r^b, H_j^b\}$. The medium parameters of the background are given by the conductivity σ_b , permittivity ε_b , and permeability $\mu_b = \mu_0$.

We subsequently place a dielectric object within the scanner. The object occupies a bounded subdomain \mathbb{D} of \mathbb{R}^3 and is characterised by a conductivity $\sigma(\mathbf{x})$, permittivity $\varepsilon(\mathbf{x})$, and permeability $\mu = \mu_0$. The total RF field that is now present within the scanner is written as $\{E_r, H_j\}$ and the scattered field is introduced as

$$E_r^{\text{sc}} = E_r - E_r^b \quad \text{and} \quad H_j^{\text{sc}} = H_j - H_j^b \quad (1)$$

for all $\mathbf{x} \in \mathbb{R}^3$. In other words, the dielectric body serves as a source for the scattered electromagnetic field. Explicitly, by using the linearity of Maxwell's equations, we find that the scattered magnetic field strength due to the object is given by the integral representation [29]

$$H_j^{\text{sc}}(\mathbf{x}) = \int_{\mathbf{x}' \in \mathbb{D}} G_{j,r}^{\text{HJ}}(\mathbf{x}, \mathbf{x}') w_r(\mathbf{x}') dV, \quad \mathbf{x} \in \mathbb{R}^3, \quad (2)$$

while the scattered electric field strength is given by

$$E_k^{\text{sc}}(\mathbf{x}) = \int_{\mathbf{x}' \in \mathbb{D}} G_{k,r}^{\text{EJ}}(\mathbf{x}, \mathbf{x}') w_r(\mathbf{x}') dV, \quad \mathbf{x} \in \mathbb{R}^3. \quad (3)$$

In these representations, $G_{j,r}^{\text{HJ}}$ and $G_{k,r}^{\text{EJ}}$ are the electric current to magnetic field and electric current to electric field Green's tensors given by

$$G_{j,r}^{\text{HJ}}(\mathbf{x}, \mathbf{x}') = \eta_b \epsilon_{jmr} \partial_m \frac{\exp(-\gamma |\mathbf{x} - \mathbf{x}'|)}{4\pi |\mathbf{x} - \mathbf{x}'|} \quad (4)$$

and

$$G_{k,r}^{\text{EJ}}(\mathbf{x}, \mathbf{x}') = (\partial_k \partial_r - \gamma^2 \delta_{kr}) \frac{\exp(-\gamma |\mathbf{x} - \mathbf{x}'|)}{4\pi |\mathbf{x} - \mathbf{x}'|}, \quad (5)$$

where δ_{kr} is the Kronecker delta, ϵ_{jmr} the completely anti-symmetric Levi Civita tensor, $\eta_b = \sigma_b - i\omega \varepsilon_b$ the so-called per-unit-length admittance of the background medium, and $\gamma = [-i\omega \mu_0 \eta_b]^{1/2}$ with $\text{Re}(\gamma) \geq 0$. Furthermore, w_r is the contrast source given by

$$w_r = \chi E_r, \quad (6)$$

where $\chi(\mathbf{x}) = \eta/\eta_b - 1$ is the contrast function and $\eta(\mathbf{x}) = \sigma(\mathbf{x}) - i\omega \varepsilon(\mathbf{x})$ is the per-unit-length admittance of the object. Obviously, the contrast function χ is unknown and our goal is to reconstruct this function by inverting measured B_1^+ data.

To this end, we first introduce a so-called data operator that relates B_1^+ scattered field data to the contrast source w_r . Using the integral representation of (2) and assuming that B_1^+ measurements are carried out within a bounded measurement domain \mathbb{S} , we find

$$B_1^{\text{sc};+}(\mathbf{x}) = \frac{B_1^{\text{sc}}(\mathbf{x}) + iB_2^{\text{sc}}(\mathbf{x})}{2} = G_{\mathbb{S}}\{w_r\}(\mathbf{x}), \quad (7)$$

where we have introduced the B_1^+ data operator $G_{\mathbb{S}}$ as

$$G_{\mathbb{S}}\{w_r\}(\mathbf{x}) = \frac{\mu_0}{2} \int_{\mathbf{x}' \in \mathbb{D}} [G_{1,r}^{\text{HJ}}(\mathbf{x}, \mathbf{x}') + iG_{2,r}^{\text{HJ}}(\mathbf{x}, \mathbf{x}')] w_r(\mathbf{x}') dV, \quad (8)$$

with $\mathbf{x} \in \mathbb{S}$. Equation (7) relates the scattered B_1^+ field to the contrast source w_r via the electric current to magnetic field Green's tensor $G_{j,r}^{\text{HJ}}$ of the background medium and is known as the *data equation*. In practice, the background field can be

obtained through field measurements in an empty coil or via simulations. In both cases, the background field is not known exactly, of course. Measurements are affected by measurement errors and noise, for example, while in simulations the model that is used to determine the background field should be sufficiently accurate. In this paper and in [23], a simple line source model is used to simulate the background field in the midplane of an empty coil, which is sufficient so long as the field in the midplane is considered (as demonstrated in [27]). Variations due to noise can be taken into account by regularizing the CSI objective function as described below.

By definition, the contrast source consists of the product of the contrast function and the total electric field strength inside the object (see (6)). This electric field strength is unknown, of course, but we do have the integral representation of (3) at our disposal. In particular, by restricting the observation vector to the object domain \mathbb{D} and by using the definition of the scattered electric field, we know that the total electric field inside the object must satisfy the equation

$$E_k(\mathbf{x}) - \int_{\mathbf{x}' \in \mathbb{D}} G_{k,r}^{\text{EJ}}(\mathbf{x}, \mathbf{x}') w_r(\mathbf{x}') dV = E_k^{\text{b}}(\mathbf{x}) \quad (9)$$

with $\mathbf{x} \in \mathbb{D}$. Observe that for a given contrast χ this is an integral equation for the total electric field strength E_r inside the object domain \mathbb{D} . Multiplying the above equation by the contrast function χ , we arrive at the so-called *object equation*

$$w_k(\mathbf{x}) - \chi(\mathbf{x}) \int_{\mathbf{x}' \in \mathbb{D}} G_{k,r}^{\text{EJ}}(\mathbf{x}, \mathbf{x}') w_r(\mathbf{x}') dV = \chi(\mathbf{x}) E_k^{\text{b}}(\mathbf{x}), \quad (10)$$

with $\mathbf{x} \in \mathbb{D}$, which can also be written as

$$w_k(\mathbf{x}) - \chi(\mathbf{x}) G_{\text{D};k}\{w_r\}(\mathbf{x}) = \chi(\mathbf{x}) E_k^{\text{b}}(\mathbf{x}), \quad \text{with } \mathbf{x} \in \mathbb{D}, \quad (11)$$

where we have introduced the object operator as

$$G_{\text{D};k}\{w_r\}(\mathbf{x}) = \int_{\mathbf{x}' \in \mathbb{D}} G_{k,r}^{\text{EJ}}(\mathbf{x}, \mathbf{x}') w_r(\mathbf{x}') dV \quad (12)$$

with $\mathbf{x} \in \mathbb{D}$. To summarize, the data equation (7) relates the contrast source to scattered B_1^+ data collected on a measurement domain \mathbb{S} , while the object equation of (11) must be satisfied for the exact contrast function and the corresponding total electric field strength. Finally, for later reference we introduce an inner product on the measurement domain \mathbb{S} as

$$\langle f, g \rangle_{\mathbb{S}} = \int_{\mathbf{x} \in \mathbb{S}} f(\mathbf{x}) \bar{g}(\mathbf{x}) dV, \quad (13)$$

where the overbar denotes complex conjugation. This inner product induces a norm given by $\|f\|_{\mathbb{S}} = \langle f, f \rangle_{\mathbb{S}}^{1/2}$. Similarly, for two vector functions u_k and v_k defined on the object domain \mathbb{D} , we define their inner product as

$$\langle u_k, v_k \rangle_{\mathbb{D}} = \int_{\mathbf{x} \in \mathbb{D}} u_k(\mathbf{x}) \bar{v}_k(\mathbf{x}) dV. \quad (14)$$

This inner product induces a norm $\|u_k\|_{\mathbb{D}} = \langle u_k, u_k \rangle_{\mathbb{D}}^{1/2}$.

A. The Contrast Source Inversion Method

Having introduced the necessary operators and inner products, we are now in a position to set up the CSI method.

For an arbitrary contrast function χ and contrast source w_r , we start by defining the data and object residual as

$$\rho(\mathbf{x}) = B_1^{+;\text{sc}}(\mathbf{x}) - G_{\text{S}}\{w_r\}(\mathbf{x}), \quad \mathbf{x} \in \mathbb{S}, \quad (15)$$

and

$$r_k(\mathbf{x}) = \chi(\mathbf{x}) E_k^{\text{b}}(\mathbf{x}) - w_k(\mathbf{x}) + \chi G_{\text{D};k}\{w_r\}(\mathbf{x}), \quad \mathbf{x} \in \mathbb{D}, \quad (16)$$

respectively. Note that using (9), the object residual can also be written as $r_k(\mathbf{x}) = \chi(\mathbf{x}) E_k(\mathbf{x}) - w_k(\mathbf{x})$. Both residuals are used to measure the discrepancy in satisfying the data and object equation. Specifically, for the data equation we use the objective function

$$F_{\text{S}}(w_r) = \frac{\|\rho\|_{\mathbb{S}}^2}{\|B_1^{+;\text{sc}}\|_{\mathbb{S}}^2}, \quad (17)$$

while for the object equation we use

$$F_{\text{D}}(w_r, \chi) = \frac{\|r_k\|_{\mathbb{D}}^2}{\|\chi E_k^{\text{b}}\|_{\mathbb{D}}^2}. \quad (18)$$

In (15) the $B_1^{+;\text{sc}}$ is the scattered B_1^+ field obtained via measurements and $G_{\text{S}}\{w_r\}$ is the estimated modeled data. In practice, $B_1^{+;\text{sc}}$ is obtained by subtracting the background field from the total B_1^+ field. In the CSI method, the total objective function

$$F(w_r, \chi) = F_{\text{S}}(w_r) + F_{\text{D}}(w_r, \chi) \quad (19)$$

now serves as a starting point to iteratively obtain reconstructions of the true contrast function and true contrast source. In particular, suppose that at the start of the n th iteration of the CSI method we have available a contrast source $w_r^{[n-1]}$ and contrast function $\chi^{[n-1]}$. At every iteration, the CSI method updates both the contrast source and the contrast function using a two-step updating procedure. Specifically, in the first step the contrast function remains fixed ($\chi = \chi^{[n-1]}$) and the contrast source is updated using the conjugate-gradient update formula

$$w_r^{[n]} = w_r^{[n-1]} + \alpha^{[n]} v_r^{[n]}, \quad (20)$$

where $\alpha^{[n]}$ is the step length and the $v_r^{[n]}$ are the so-called Polak-Ribière [28] update directions given by

$$v_r^{[n]} = g_r^{[n]} + \frac{\text{Re} \langle g_r^{[n]}, g_r^{[n]} - g_r^{[n-1]} \rangle_{\mathbb{D}}}{\|g_r^{[n-1]}\|_{\mathbb{D}}^2} v_r^{[n-1]}, \quad (21)$$

with $v_r^{[0]} = 0$. In the above equation, $g_r^{[n]}$ is the gradient of the objective function with respect to the contrast source w_r evaluated at $w_r = w_r^{[n-1]}$ and $\chi = \chi^{[n-1]}$. This gradient can be computed in a straightforward fashion and an explicit expression can be found in [30], for example. Having the

gradient and new update direction r available, the step length $\alpha^{[n]}$ is determined as

$$\alpha^{[n]} = \underset{\alpha \in \mathbb{R}}{\operatorname{argmin}} F^{[n]} \left(w_r^{[n-1]} + \alpha v_r^{[n]}, \chi^{[n-1]} \right) \quad (22)$$

and an explicit expression for $\alpha^{[n]}$ can be found in [30] as well.

In the second step of the CSI method, we use the updated contrast source $w_r^{[n]}$ to obtain a new contrast function $\chi^{[n]}$. In particular, we first compute the electric field strength that corresponds to the newly obtained contrast source using the formula (see (9))

$$E_k^{[n]} = E_k^b + G_{D,k} \left\{ w_r^{[n]} \right\} \quad (23)$$

and subsequently determine the contrast function by minimizing

$$F_D^{[n]} \left(w_r^{[n]}, \chi \right) = \frac{\|r_k\|_D^2}{\|\chi^{[n-1]} E_k^b\|_D^2} \quad (24)$$

with respect to χ with $E_k = E_k^{[n]}$. The new contrast is then obtained as

$$\chi^{[n]} = \frac{w_k^{[n]} \bar{E}_k^{[n]}}{E_k^{[n]} \bar{E}_k^{[n]}}. \quad (25)$$

We have now completely described our initial version of the CSI method. Further refinements with a focus on an MRI setting are given below. Before doing so, however, first observe that apart from the contrast, the method also reconstructs the electric field strength via (23) which is extremely important in determining the Specific Absorption Rate. Furthermore, the method should start with a nonzero initial guess for the contrast function χ , since the second term of the objective function is undefined at $\chi = 0$. A common choice is to use the contrast function that is obtained by simple backpropagation (see [30]), but any other nonzero initial guess, such as an original EPT reconstruction, may be used as well. Simply backpropagation essentially amounts to applying the adjoint of the data operator on the data and is described in [24], [26], and [30], for example.

B. Multiple Antenna Settings and Multiplicative Regularization

Having described the basic CSI method, we now introduce two further refinements that allow us to apply the method in a practical MRI setting. First, we like to incorporate possible complementary antenna settings as used in a single MRI experiment. This adjustment is fairly straightforward to implement. Specifically, to incorporate $J \geq 1$ different antenna settings in the CSI method, we again use an objective function of the form $F_n = F_S + F_{D,n}$ at every iteration, but this time F_S and $F_{D,n}$ are given by

$$F_S = \frac{\sum_{j=1}^J \|\rho(j)\|_S^2}{\sum_{j=1}^J \|B_1^{+;sc}(j)\|_S^2} \quad (26)$$

$$F_D^{[n]} = \frac{\sum_{j=1}^J \|r_k(j)\|_D^2}{\sum_{j=1}^J \|\chi^{[n-1]} E_k^b(j)\|_D^2}, \quad (27)$$

where $\rho(j)$ and $r_k(j)$ are the data and object residuals for the j th antenna setting, respectively, while $B_1^{+;sc}(j)$ denotes the corresponding scattered B_1^+ field and $E_k^b(j)$ the corresponding background electric field strength. Gradients, update directions, and step lengths can now be computed in essentially the same manner as in the single antenna setting case.

As second refinement, we incorporate a multiplicative regularization term to suppress the effects of noise on the reconstruction results. In particular, we follow [30] and minimize the objective function

$$F^{[n]} = \left[F_S + F_D^{[n]} \right] \cdot F_{TV}^{[n]}(\chi), \quad (28)$$

at the n th iteration, where

$$F_{TV}^{[n]}(\chi) = \frac{\int_{\mathbf{x} \in \mathbb{D}} \left(|\nabla \chi(\mathbf{x})|^2 + \delta_{[n-1]}^2 \right) dV}{\int_{\mathbf{x} \in \mathbb{D}} \left(|\nabla \chi^{[n-1]}(\mathbf{x})|^2 + \delta_{[n-1]}^2 \right) dV} \quad (29)$$

is our multiplicative regularization term and F_S and $F_D^{[n]}$ are given by (26) and (27), respectively. In the above expression, the parameter $\delta_{[n-1]}^2$ is chosen as (see [30])

$$\delta_{[n-1]}^2 = F_{D,n-1} \Delta^2, \quad (30)$$

where Δ is the reciprocal of the mesh size used to discretize the object domain \mathbb{D} . Furthermore, since $F_n^{TV}(\chi^{[n-1]}) = 1$, we observe that the first step of the CSI method is unaffected by the inclusion of the total regularization term and only the second step needs to be modified. In particular, the second step of the CSI method now consists of updating the contrast function according to the update formula

$$\chi^{[n]} = \chi^{[n-1]} + \alpha_\chi^{[n]} d^{[n]}, \quad (31)$$

where the Polak-Ribière [28] update directions for the contrast are given by

$$d^{[n]} = g_\chi^{[n]} + \frac{\operatorname{Re} \left\langle g_\chi^{[n]}, g_\chi^{[n]} - g_\chi^{[n-1]} \right\rangle_D}{\|g_\chi^{[n-1]}\|_D^2} d^{[n-1]} \quad (32)$$

with $d^{[0]} = 0$ and $g_\chi^{[n]}$ is a preconditioned gradient of F_n with respect to the contrast function χ evaluated at $w_r = w_r^{[n]}$ and $\chi = \chi^{[n-1]}$ (see [30]). Note that by following this approach, the above updating scheme for the contrast reduces to the standard CSI method in case total variation regularization is switched off ($F_{TV}^{[n]} = 1$). Finally, with the gradients and update directions at our disposal, the step length $\alpha_\chi^{[n]}$ can be determined as

$$\alpha_\chi^{[n]} = \underset{\alpha \in \mathbb{R}}{\operatorname{argmin}} F^{[n]} \left(w_r^{[n]}, \chi^{[n-1]} + \alpha d^{[n]} \right). \quad (33)$$

With these two refinements, we have arrived at our final CSI method. The method is summarized below and we are now in a position to apply the method in a practical MRI setting.

CSI Method with regularization

- Given an initial contrast source $w_r^{[0]}$ and a nonzero initial contrast $\chi^{[0]}$
- For $n = 1, 2, \dots$
 - **Step 1: Update the contrast source**
 - 1) Compute the gradient of the objective function with respect to w_r at $w_r = w_r^{[n-1]}$ and $\chi = \chi^{[n-1]}$
 - 2) Compute the Polak-Ribière update direction $v_r^{[n]}$
 - 3) Compute the step length $\alpha^{[n]}$
 - 4) Determine the new contrast source $w_r^{[n]} = w_r^{[n-1]} + \alpha^{[n]} v_r^{[n]}$
 - **Step 2: Update the contrast function**
 - 1) Compute the preconditioned gradient of the objective function with respect to χ at $w_r = w_r^{[n]}$ and $\chi = \chi^{[n-1]}$
 - 2) Compute $d^{[n]}$, the Polak-Ribière update direction for the contrast
 - 3) Compute the step length $\alpha_\chi^{[n]}$
 - 4) Determine the new contrast function $\chi^{[n]} = \chi^{[n-1]} + \alpha_\chi^{[n]} d^{[n]}$
 - Stop if $F^{[n]} <$ user specified tolerance level
OR
 - Stop if $n =$ user specified number of iterations
- End

III. NUMERICAL RESULTS

The results presented in this paper are based on a two-dimensional configuration in which only H_x , H_y and E_z are excited (E-polarized fields). Simulations were performed using 16 RF line sources driven at 128 MHz, which corresponds to an operating frequency of the RF body coil in a 3 T MR system. The line sources were located on a circle ($r = 0.34$ m) symmetrically positioned around a slice of a female pelvis model (Ella model, ITIS Foundation [33]) with an isotropic voxel size of 1.0 mm. A homogeneous medium is taken as a background model (no RF shield is taken into account) and the assigned conductivity and permittivity values are based on [34] at 128 MHz. Three different RF excitation settings were used to acquire the EM fields as illustrated in Fig. 1(a)–(c). In Fig. 1(d)–(f) and (g)–(i) are shown the $|B_1^+|$ -maps and the $|E|$ -fields, respectively, for the electric conductivity and permittivity maps of the pelvis model as depicted in Fig. 2(a), (b). The presented fields in Fig. 1 are noiseless and only the B_1^+ fields (amplitude and phase) were used as an input to CSI-EPT. To test the presented CSI-EPT algorithm, the B_1^+ fields with additive Gaussian noise (SNR 20) were used as input.

In Fig. 3(a), (b) and (c), (d), the reconstructed maps obtained after 1000 and 10000 iterations, respectively, are shown based on noiseless B_1^+ data using a quadrature phase setting (see Fig. 1(a)). We observe that the conductivity and permittivity profile reconstructions after 1000 iterations are fairly accurate, but the reconstructed values of small tissue structures (e.g., vessels) are underestimated. Furthermore, there is a reconstruction error around the central part of the anatomy and a noticeable

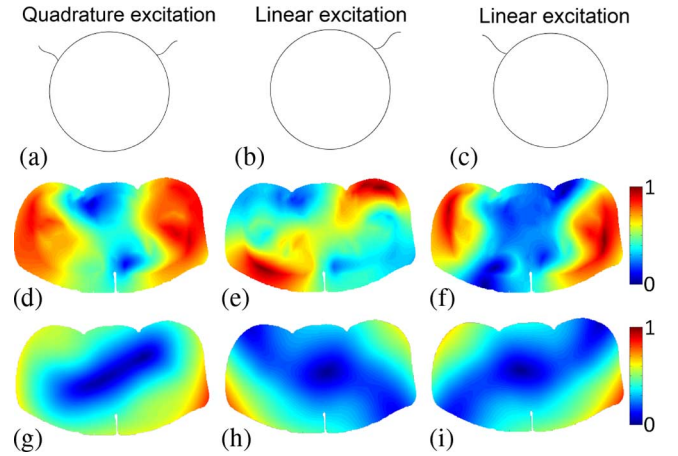


Fig. 1. Three different RF excitation modes (top row) and the corresponding amplitude of B_1^+ fields (middle row) and the amplitude of electric fields (bottom row). The color bars indicate normalized field values.

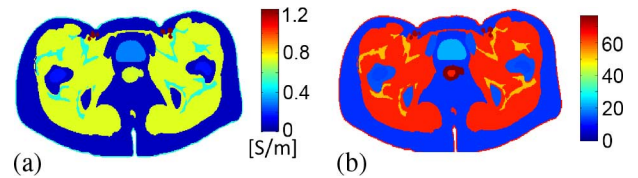


Fig. 2. Electric conductivity (a) and permittivity (b) map of the actual female pelvis model.

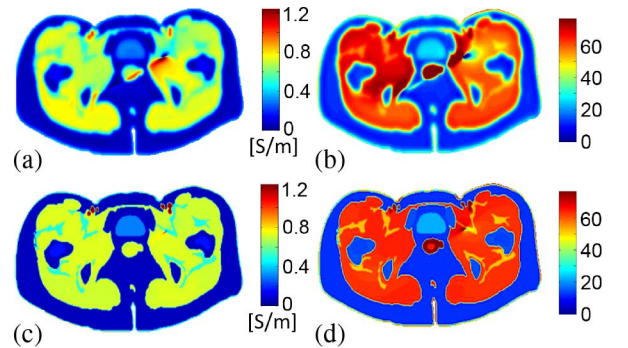


Fig. 3. The reconstructed conductivity and permittivity maps based on noiseless B_1^+ data after 1000 iterations (a), (b) and after 10000 iterations (c), (d).

overestimation is observed under the diagonal of the anatomy. The reconstructed maps after 10000 iterations, however, are highly accurate and in good agreement with the actual model. Fine structures are resolved and reliable results are produced near interfaces between different tissue types. Continuing the iterative process for more than 10000 iterations did not further improve the results and, in practice, the stopping condition can be set in terms of a tolerance level on the the objective function or in terms of the number of iterations.

The reconstructed maps after 1000 iterations based on noisy B_1^+ data for the quadrature phase setting (Fig. 1(a)), are shown in Fig. 4(a), (b). Here, the basic implementation of CSI-EPT was used, thus without the multiplicative regularization term. In the next row (Fig. 4(c), (d)) the reconstructed maps based on the same phase setting are presented, however, here the multiplicative regularized CSI-EPT, as introduced in this paper, was

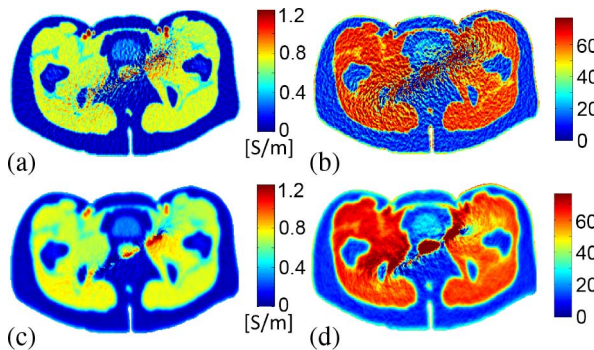


Fig. 4. Reconstructions based on noisy B_1^+ data associated with quadrature RF excitation mode using the basic CSI-EPT (a), (b) and the presented implementation with Total Variation factor (c), (d) after 1000 iterations.

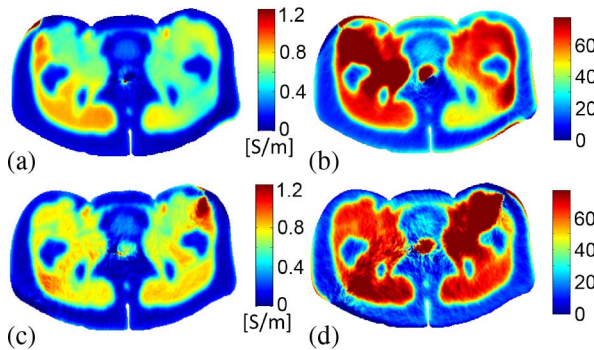


Fig. 5. (a), (b) Reconstruction results based on fields acquired with linear RF excitation mode as depicted in Fig. 1(b). (c), (d) Reconstructed maps based on fields using linear RF excitation mode as shown in Fig. 1(c). These reconstructions are obtained after 1000 iterations.

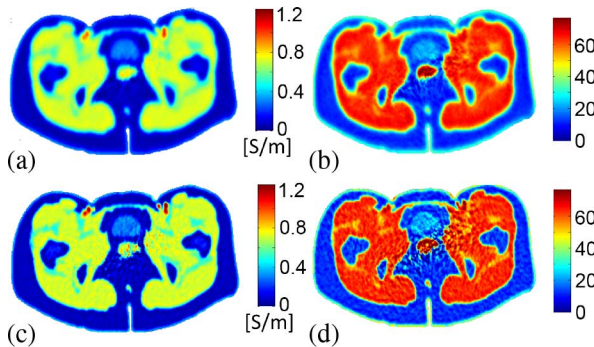


Fig. 6. The reconstructed maps after 1000 (a), (b) and 5000 iterations (c), (d) using three B_1^+ data sets as input to the presented algorithm.

used. It is observed that the reconstructed values on the diagonal of the pelvis region show deviation from the true values. This region coincides with the low $|E|$ -field strength associated with quadrature excitation as observed in Fig. 1(g). When using B_1^+ data acquired in a linear excitation mode (Fig. 1(b)), the observed artifacts are positioned on the other diagonal of the pelvis as depicted in Fig. 5(a), (b). Similarly, there is a correlation between the region of less reliable reconstruction and the region of low $|E|$ -field as observed in Fig. 1(h). Reconstructions based on a complementary antenna setting (Fig. 1(c)) show that the artifacts (Fig. 5(c), (d)) are located on a different region compared to reconstructions based on previous two RF excitation settings.

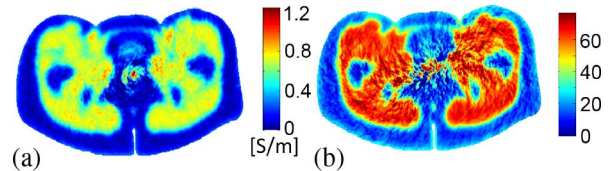


Fig. 7. The reconstructed maps after 1000 iterations using three B_1^+ data sets with transceive phase as input.

By using the complete B_1^+ data set, acquired by these three excitation settings, as input to the presented algorithm, the reconstructed maps, as shown in Fig. 6(a), (b), are obtained (again after 1000 iterations). If the iterative process is continued up to 5000 iterations, then the reconstruction results, as depicted in Fig. 6(c), (d) are obtained. It is observed (Fig. 6(c), (d)) that the edges are sharper compared to the reconstruction results after 1000 iterations.

To visualize the performance of CSI-EPT on tissue interfaces, line profiles of the reconstructed maps of Fig. 3(a)–(d), 4(a)–(d), 6(c) and (d) have been depicted in Fig. 8. The mean \pm standard deviation of the reconstructed electric properties of four tissue types (muscle, bladder, fat and bone) are presented in Fig. 9. Calculation of the mean \pm standard deviation is based on true model tissue segmentation where all voxels of the forementioned tissue type are included. In Fig. 9 it can be observed that the reconstructed mean values after 10000 iterations (light blue) are in better agreement with true values compared to the reconstructed mean values after 1000 iterations (green). Furthermore, it is observed that the standard deviation is smaller after 10000 iterations. The reconstructed mean values based on noisy data (red) are in good agreement with the true values as well, and the standard deviation is relatively low due to the use of the multiplicative term (TV-term). Finally, the results using three B_1^+ data sets and increased number of iterations show an improvement in terms of standard deviation for all tissue types (purple).

In Fig. 7 the reconstruction results after 1000 iterations are shown in case regularized CSI-EPT is applied on B_1^+ amplitude and transceive phase data. The input data was acquired using the three different excitation modes and additive Gaussian noise (SNR 20) was added. The reconstruction results show a deviation from the true maps around the central region of the slice. Moreover, the reconstructions suffer from a loss of resolution, since small structures are not completely resolved.

The computational time for 1000 iterations of a Matlab implementation of the presented method, with a grid size of 1.0 mm, is around 90 seconds on an Intel Core i7 operating at 1.9 GHz.

IV. DISCUSSION AND CONCLUSION

In this paper, we have presented a multiplicative regularized Contrast Source Inversion approach for improved MRI based electric properties mapping. The method takes the integral representations for the electromagnetic field as a starting point and the tissue parameters are obtained by iteratively minimizing an objective function which measures the discrepancy between measured and modeled data and the discrepancy in satisfying a consistency equation known as the object equation. Furthermore, the objective function consists of a multiplicative Total

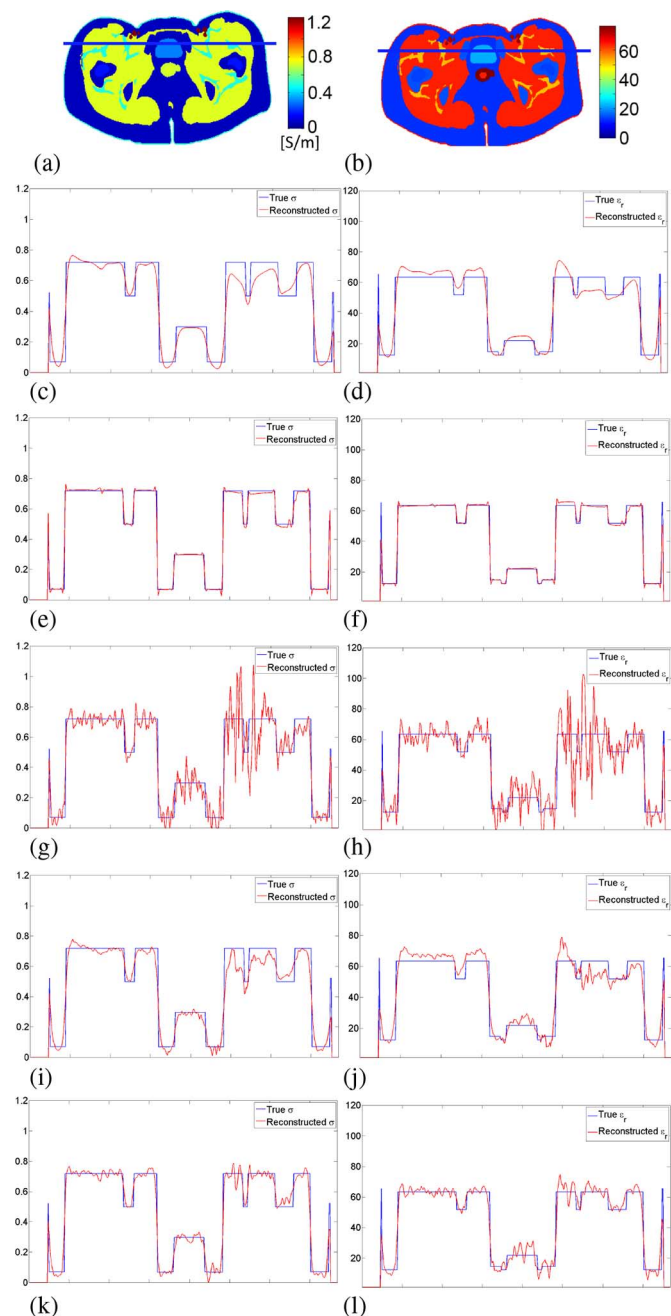


Fig. 8. (a), (b) Line position w.r.t. the true model. (c), (d) and (e), (f) Line profiles of the reconstructed maps as depicted in Fig. 3(a), (b) and (c), (d), respectively. (g), (h) and (i), (j) Line profiles of the reconstructed maps of Fig. 4(a), (b) and (c), (d), respectively. (k), (l) Line profile of the reconstruction results as depicted in Fig. 6(c), (d). The x-axes in these figures correspond to the line in Figs. 8(a) and (b), while along the y-axes the conductivity [S/m] (left column) or the relative permittivity (right column) is shown.

Variation factor for noise suppression during the reconstruction process. Finally, the presented implementation of the CSI-EPT method is able to simultaneously utilize more than one B_1^+ data set acquired by complementary RF excitation settings.

Numerical results illustrate that fine structures can be resolved and the method performs well at tissue boundaries as shown in Figs. 3–9. The reconstructed electric properties based on noiseless B_1^+ data are in good agreement with true electric properties already after 1000 iterations (Fig. 3(a), (b) and

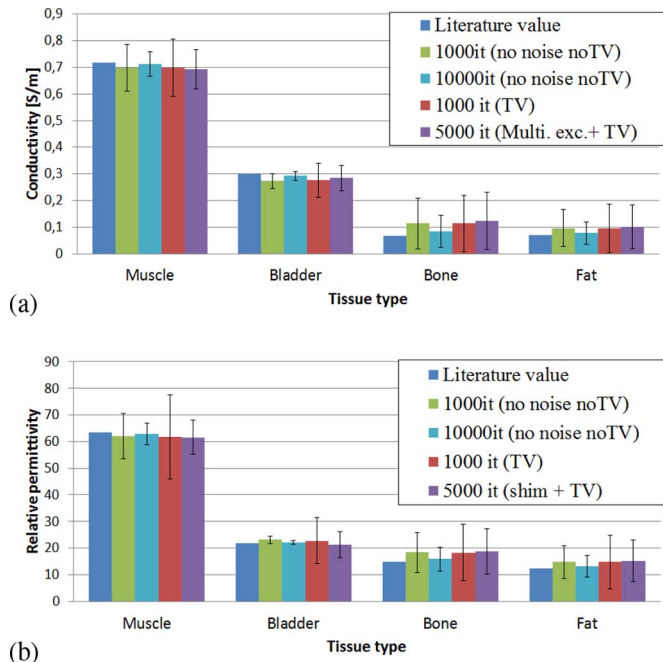


Fig. 9. Average conductivity (a) and permittivity values (b) for various tissue types (muscle, bladder, bone, fat) based on quadrature excitation (green, light blue, red) and based on three RF excitation settings (purple). Green bar corresponds to Fig. 3(a), (b), light blue to Fig. 3(c), (d), red to Fig. 4(c), (d) and purple to Fig. 6(c), (d). The values based on literature are depicted in dark blue.

8(c), (d)). The good performance of the presented method is observed after 10000 iterations where the reconstructed maps (Fig. 3(c), (d)) are in very good agreement with the true model. The line profiles presented in 8(e), (f) confirm the ability of CSI-EPT to reconstruct EPs near tissue interfaces. These results clearly illustrate the improvement of CSI-EPT reconstructions at tissue boundaries compared to the currently used reconstruction algorithms. For a comparison, see [16] (Fig. 7) where boundary artifacts are observed in EPT-results of a similar slice of the Ella model.

Reconstructed maps based on noisy B_1^+ data (Fig. 4(a), (b)), using the basic implementation of CSI-EPT without noise suppression capabilities show an overall reliable reconstruction of average electric property values as shown in Fig. 9 (red bar). However, the reconstructed values were less reliable in a region that coincided with a region of low $|E|$ -fields. The line profiles (Fig. 8(g), (h)) show a larger deviation from the true values on the right part of the line profiles, due to the artifacts on the diagonal of the anatomy (Fig. 4(a), (b)). It is observed that the reconstructed maps are improved when Total Variation term is added to the CSI-EPT algorithm (Fig. 4(c), (d)). In this figure, the unreliable region is smaller and the reconstructed maps are less noisy compared to Fig. 4(a), (b). The line profiles (Fig. 8(i), (j)) confirm the improvement where it can be observed that the deviation of the reconstructed values from true values is smaller compared to the case where the TV-term was not included in the algorithm (Fig. 8(g), (h)). However, some artifacts are still observed on the diagonal of the anatomy. As the induced current is low in this region, due to a low $|E|$ -field, there is less information available to reconstruct the property maps. The region of low $|E|$ -fields can be positioned elsewhere

by using a one-port RF excitation mode as shown in the 2nd and 3rd column of Fig. 1. In practice, a complementary $|E|$ -pattern can also be achieved by varying the phase difference between the available channels of an RF transmit array. Reconstructed maps based on these input B_1^+ data, therefore, show artifacts located in other regions (Fig. 5(a)–(d)) compared to reconstructed maps using quadrature RF excitation. When using B_1^+ -fields of three different RF excitation modes (Fig. 1(a)–(c)) simultaneously, an overall improvement is observed in the reconstructed maps (Fig. 6(a), (b)) where the region sensitive to noise has been reduced to a few pixels around the central part of the anatomy. Sharper edges are reconstructed if the iteration procedure is continued to 5000 iterations as shown in Fig. 6(c), (d). An improvement is also observed in terms of average and deviation of the reconstructed values for various tissue types as observed in 8(k), (l) and Fig. 9 (purple bar). Furthermore, reconstruction results based on transceive phase data (Fig. 7) show local deviations from the actual property maps and loss of resolution (small structures are not completely resolved). A modification of the CSI objective function, which takes uncertainties in the phase of B_1^+ into account, may resolve these problems (cf. [32]).

In its present form, however, CSI-EPT does not include the RF shield in the Green's function. Future work will therefore focus on use of the Green's function in which the RF shield is included analytically or numerically as presented in [35]. Finally, we mention that uncertainties in the B_1^+ phase may also be taken into account by modifying the objective function that is minimized in the CSI-EPT method. In practice, measurements of the B_1^+ phase are based on assumptions regarding the object and coil geometry [11], [13]. The transceive phase assumption can be considered as an uncertainty in the B_1^+ phase, and, therefore, be incorporated in the objective function. Recent studies [14], [15], [36]–[40] avoid the transceive phase assumption by using multiple independent transmit/receive channels and open up possibilities for EPT reconstruction and local SAR estimation [36], [39], [40], free of assumption regarding the B_1^+ phase. Modern 3 T clinical MRI systems are often equipped with at least two independent transmit channels for RF shimming purposes, therefore field patterns as shown in Fig. 1 can be generated. Desirable field patterns can be achieved such that low $|E|$ -field regions do not overlap with the low field regions acquired by the complementary phase settings. As the artifacts in the reconstruction results based on three different B_1^+ -fields were reduced to a few pixels, additional B_1^+ data might not be required for the current possible applications of CSI-EPT.

The applicability of the EPT method to electric properties mapping has recently been confirmed in a series of phantom and in vivo experiments with MRI systems [11]–[19], [12], [38] and it is certainly our intention to extend the current implementation of CSI-EPT towards a practical MRI setting. Much effort is still needed, however. Specifically, the method needs to be extended to 3D and the effect of the RF shield needs to be taken into account either numerically or analytically. A 3D implementation requires the implementation of the fully vectorial 3D scattering operators and will obviously increase CPU processing time due to an increase in the number of unknowns and the use of 3D FFTs. Finally, perturbations in the phase of the B_1^+ field can be taken into account by modifying the CSI objective function in

a similar manner as in [32]. Given the promising results presented in this paper, we think that CSI-EPT may prove an important step forward and may greatly improve the reliability of EPT as a functional mapping technique. Furthermore, since the method is also able to reconstruct the electric field, it can in principle provide all relevant information for local SAR estimation as well.

REFERENCES

- [1] M. de Greef, H. P. Kok, D. Correia, A. Bel, and J. Crezee, "Uncertainty in hyperthermia treatment planning: The need for robust system design," *Phys. Med. Biol.*, vol. 56, no. 11, pp. 3233–3250, 2011.
- [2] J. C. Lin, *Advances in Electromagnetic Fields in Living Systems*. Hoboken, NJ: Springer, 2005.
- [3] W. T. Joines, Y. Zhang, C. Li, and R. L. Jirtle, "The measured electrical properties of normal and malignant human tissues from 50 to 900 MHz," *Med. Phys.*, vol. 21, pp. 547–550, 1994.
- [4] A. J. Surowiec, S. S. Stuchly, J. B. Barr, and A. Swarup, "Dielectric properties of breast carcinoma and the surrounding tissues," *IEEE Trans. Biomed. Eng.*, vol. 35, no. 4, pp. 257–263, Apr. 1988.
- [5] P. R. Stauffer, F. Rossetto, M. Prakash, D. G. Neuman, and T. Lee, "Phantom and animal tissues for modelling the electrical properties of human liver," *Int. J. Hyperthermia*, vol. 19, pp. 89–101, 2003.
- [6] A. P. O'Rourke *et al.*, "Dielectric properties of human normal, malignant and cirrhotic liver tissue: in vivo and ex vivo measurements from 0.5 to 20 GHz using a precision open-ended coaxial probe," *Phys. Med. Biol.*, vol. 52, pp. 4707–4719, 2007.
- [7] A. Keshtkar, Z. Salehnia, A. Keshtkar, and B. Shokouhi, "Bladder cancer detection using electrical impedance technique (Tabriz Mark 1)," *Patholog. Res. Int.*, 2012.
- [8] Y. Lu, B. Li, J. Xu, and J. Yu, "Dielectric properties of human glioma and surrounding tissue," *Int. J. Hyperthermia*, vol. 8, pp. 755–760, 1992.
- [9] E. M. Haacke, L. S. Petropoulos, E. W. Nilges, and D. H. Wu, "Extraction of conductivity and permittivity using magnetic resonance imaging," *Phys. Med. Biol.*, vol. 36, no. 6, pp. 723–734, 1991.
- [10] H. Wen, "Non-invasive quantitative mapping of conductivity and dielectric distributions using the RF wave propagation effects in high field MRI," in *Proc. SPIE*, 2003, vol. 5030, pp. 471–477.
- [11] U. Katscher *et al.*, "Determination of electric conductivity and local SAR via B1 mapping," *IEEE Trans. Med. Imag.*, vol. 28, no. 9, pp. 1365–1375, Sep. 2009.
- [12] T. Voigt, U. Katscher, and O. Doessel, "Quantitative conductivity and permittivity imaging of the human brain using electric properties tomography," *Magn. Reson. Med.*, vol. 66, pp. 456–466, 2011.
- [13] A. L. van Lier *et al.*, " B_1^+ phase mapping at 7 T and its application for in vivo electrical conductivity mapping," *Magn. Reson. Med.*, vol. 67, no. 2, pp. 552–561, 2011.
- [14] D. K. Sodickson *et al.*, "Generalized local Maxwell tomography for mapping of electrical property gradients and tensors," in *Proc. 21th Annu. Meet. ISMRM*, Salt Lake City, UT, 2013, p. 4175.
- [15] J. Liu, X. Zhang, P. F. van de Moortele, S. Schmitter, and B. He, "Determining electrical properties based on B1 fields measured in an MR scanner using a multi-channel transmit/receive coil: A general approach," *Phys. Med. Biol.*, vol. 58, pp. 4395–4408, 2013.
- [16] E. Balidemaj *et al.*, "Feasibility of electric property tomography of pelvic tumors at 3 T," *Magn. Reson. Med.*, vol. 73, no. 4, pp. 1505–1513, Apr. 2014.
- [17] J. K. Seo, M. O. Kim, J. Lee, N. Choi, and E. J. Woo, "Error analysis of nonconstant admittivity for MR-based electric property imaging," *IEEE Trans. Med. Imag.*, vol. 31, no. 2, pp. 430–437, Feb. 2012.
- [18] J. Liu, X. Zhang, S. Schmitter, P. F. van de Moortele, and B. He, "Gradient-based electrical properties tomography (gEPT): A robust method for mapping electrical properties of biological tissues in vivo using magnetic resonance imaging," *Magn. Reson. Med.*, 2014.
- [19] L. Huang *et al.*, "A Monte Carlo method for overcoming the edge artifacts in MRI-based electrical conductivity mapping," in *Proc. 22th Annu. Meet. ISMRM*, Milan, Italy, 2014, p. 3190.
- [20] F. S. Hafalir, O. F. Oran, N. Gurler, and Y. Z. Ider, "Convection-reaction equation based magnetic resonance electrical properties tomography (cr-MREPT)," *IEEE Trans. Med. Imag.*, vol. 33, no. 3, pp. 777–793, Mar. 2014.
- [21] E. Balidemaj *et al.*, "CSI-EPT: A novel contrast source inversion approach to EPT and patient-specific SAR based on B1+ maps," in *Proc. 21th Annu. Meet. ISMRM*, Salt Lake City, UT, 2013, p. 4178.

- [22] E. Balidemaj *et al.*, "CSI-EPT: A novel contrast source approach to MRI based electric properties tomography and patient-specific SAR," in *IEEE Int. Conf. Electromagn. Adv. Appl.*, 2013, pp. 668–671.
- [23] E. Balidemaj *et al.*, "Experimental electric field and dielectric tissue property mapping using a regularized CSI-EPT reconstruction method," in *Proc. 22th Annu. Meet. ISMRM*, Milan, Italy, 2014, p. 3252.
- [24] P. M. van den Berg and R. E. Kleinman, "A contrast source inversion method," *Inverse Problems*, vol. 13, pp. 1607–1620, 1997.
- [25] A. Abubakar and P. M. van den Berg, "Three-dimensional nonlinear inversion in cross-well electrode logging," *Radio Sci.*, vol. 33, no. 4, pp. 989–1004, July 1998.
- [26] A. Abubakar, P. M. van den Berg, and J. J. Mallorqui, "Imaging of biomedical data using a multiplicative regularized contrast source inversion method," *IEEE Trans. Microw. Theory Tech.*, vol. 50, no. 7, pp. 1761–1777, Jul. 2002.
- [27] B. van den Bergen, C. C. Stolk, J. B. van den Berg, J. J. W. Lagendijk, and C. A. T. van den Berg, "Ultra fast electromagnetic field computations for RF multi-transmit techniques in high field MRI," *Phys. Med. Biol.*, vol. 54, no. 5, pp. 1253–1264, 2009.
- [28] E. K. P. Chong and S. H. Zak, *An Introduction to Optimization*. New York: Wiley, 2013, p. 187.
- [29] A. T. de Hoop, *Handbook of Radiation and Scattering of Waves*. San Diego, CA: Academic, 1995.
- [30] P. M. van den Berg and A. Abubakar, "Contrast source inversion method: State of art," *Progr. Electromagn. Res.*, vol. 34, pp. 189–218, 2001.
- [31] A. L. H. M. W. van Lier, "Electromagnetic and thermal aspects of radiofrequency field propagation in ultra-high field MRI," Ph.D. dissertation, Utrecht, The Netherlands, 2012.
- [32] P. M. Van den Berg, *Wavefield Inversion*, A. Wirgin, Ed. New York: Springer, 1999, pp. 191–240.
- [33] A. Christ *et al.*, "The virtual family development of surface-based anatomical models of two adults and two children for dosimetric simulations," *Phys. Med. Biol.*, vol. 55, pp. 23–38, 2010.
- [34] C. G. Gabriel and E. Corthout, "The dielectric properties of biological tissues: I. Literature survey," *Phys. Med. Biol.*, vol. 41, pp. 2231–2249, 1996.
- [35] C. A. Balanis, *Advanced Engineering Electromagnetics*, 2nd ed. New York: Wiley, 2012, pp. 933–937.
- [36] U. Katscher, C. Findekle, and T. Voigt, "B1-based specific energy absorption rate determination for nonquadrature radiofrequency excitation," *Magn. Reson. Med.*, vol. 68, pp. 1911–1918, 2012.
- [37] S. Buchenau, M. Haas, D. N. Splitthoff, J. Hennig, and M. Zaitsev, "Iterative separation of transmit and receive phase contributions and B1(+)-based estimation of the specific absorption rate for transmit arrays," *Magn. Reson. Mater. Phys.*, vol. 26, pp. 463–476, 2013.
- [38] J. P. Marques, D. K. Sodickson, O. Ipek, C. M. Collins, and R. Gruetter, "Single acquisition electrical property mapping based on relative coil sensitivities: A proof-of-concept demonstration," *Magn. Reson. Med.*, 2014.
- [39] X. Zhang, P. F. van de Moortele, S. Schmitter, and B. He, "Complex B1 mapping and electrical properties imaging of the human brain using a 16-channel transceiver coil at 7 T," *Magn. Reson. Med.*, vol. 69, no. 5, pp. 1285–1296, 2013.
- [40] X. Zhang, S. Schmitter, P. F. van de Moortele, J. Liu, and B. He, "From complex mapping to local SAR estimation for human brain MR imaging using multi-channel transceiver coil at 7 T," *IEEE Trans. Med. Imag.*, vol. 32, no. 6, pp. 1058–1067, Jun. 2013.